ACS APPLIED NANO MATERIALS Cite This: ACS Appl. Nano Mater. XXXX, XXX, XXX−XXX

Article

www.acsanm.org

Mesoporous Si Nanowire Templated Controlled Fabrication of Organometal Halide Perovskite Nanoparticles with High Photoluminescence Quantum Yield for Light-Emitting Applications

Joydip Ghosh,[†] Ramesh Ghosh,[†,‡] and P. K. Giri*[,†,‡]

[†]Department of Physics and [‡]Centre for Nanotechnology, Indian Institute of Technology Guwahati, Guwahati 781039, India

Supporting Information

ABSTRACT: We report on the controlled fabrication of $CH_3NH_3PbI_3$ perovskite nanoparticles (NPs) on a mesoporous Silicon nanowire (NW) template for the first time and study the mechanism of its high photoluminescence (PL) quantum yield. Crystalline perovskite NPs are grown by spin-coating of perovskite precursor on the surface of mesoporous Si NWs fabricated by a metal-assisted chemical etching method. We have tuned the size of the perovskite NPs (5−70 nm) and its photophysical properties by controlling the porosity of the Si NWs and perovskite precursor concentrations. The as-grown perovskite NPs on Si NWs show enhancement in PL intensity by more than 1 order of magnitude as compared to that of the perovskite film on a Si substrate. Depending on the size of the perovskite NPs, the center of the PL peak of the of NPs shows a large blue-shift as compared to that of the perovskite film. A detailed systematic study reveals that decrease in particle size and the quantum confinement in perovskite NPs are primarily responsible for the enhanced yield as well as blue-shift of PL. With the help of plasma-treated Si NW template, the contribution of the photon recycling effect to the enhanced PL of NPs was quantitatively assessed and found to be only 10%. The PL quantum yield of the perovskite NPs was measured to be 9.82% as compared to the low yield (0.69%) of the perovskite film. Time-resolved PL analysis of perovskite NPs show a longer lifetime of carriers due to negligible nonraditative recombination in the NPs, which is consistent with the high PL yield. This study demonstrates an easy and cost-effective fabrication of perovskite NPs on a novel mesoporous Si NWs template, which is a versatile platform, and it unravels the mechanism behind its superior photophysical properties, which is significant for different light-emitting and display applications.

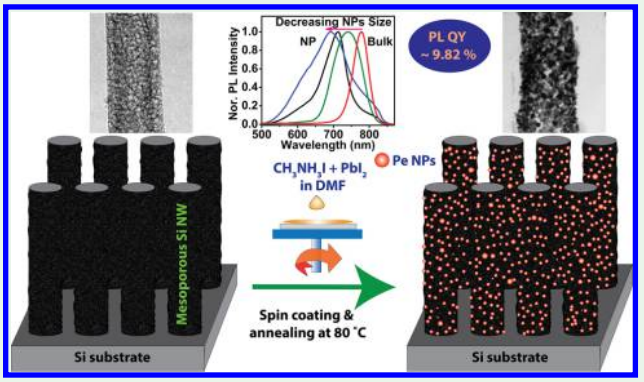

KEYWORDS: *perovskite nanoparticles, quantum yield, mesoporous Si nanowire, quantum size effect, photoluminescence*

1. INTRODUCTION

Organic−inorganic halide perovskites have drawn tremendous research attention over the past few years for their extraordinary performance in solar cell and light-emitting devices with the advantages of high absorption in the UV−vis region, low cost and low temperature processing, tunable optical band gap, and superior charge transport.[1−5] With the proper combination of electron and hole transporting layers, the power conversion efficiency of perovskite solar cell (PSC) has raised to over 22%.[1−3] Perovskites with combination of different semiconducting material have been adopted by different groups in order to improve the device performance.[6−9]

Recently, these solution-processed perovskites, especially $CH_3NH_3PbX_3$ (where, X = Cl, Br, and I), have also shown great promises in light-emitting diodes (LEDs)[10−15] and lasing applications[16] with tunable emission color by varying the halide anion.[17] In each case, the active material should show high photoluminescence (PL) emission in order to convert the generated (either electrically or optically) charges into photons efficiently. However, the application of perovskite LEDs (PeLED) and lasers is restricted due to the poor stability and low efficiency of photon emission.[18]

On the other hand, perovskite nanocrystals (NCs) have shown interesting size-dependent optical and electronic properties that differ significantly from their bulk counterparts.[19−23]Recently, colloidal and self-assembled perovskite NCs in a solid organic matrix with lower dimensionality have been reported.[18,24,25] Though these colloidal NCs show very high light emission efficiency, the luminescent NPs are necessary in solid or thin film form for practical device application. The emission intensity tends to substantially reduce when NCs are processed as thin films due to spontaneous aggregation.[26] On the other hand, the growth of perovskite NCs inside an ordered inorganic mesoporous host

Received: January 10, 2018
Accepted: March 7, 2018
Published: March 7, 2018

DOI: 10.1021/acsanm.8b00047
ACS Appl. Nano Mater. XXXX, XXX, XXX−XXX

matrix is an alternative, ligand-free route to study the effects on the optical properties due to size reduction. Interestingly, the growth of perovskite NPs using porous aluminum oxide (Al_2O_3) and silica (SiO_2) templates has been reported recently, which show very interesting optical properties due to the quantum size effect.[26−33] Recently, Zhang et al. reported a blue-shift of PL and optical band gap tuning of $CH_3NH_3PbI_3$ spin-coated on porous anodized Al_2O_3.[34] Note that the PL intensity decreases with decreasing pore size of porous Al_2O_3, while the high intensity of light emission is extremely desirable for light-emitting applications.[34] Thus, it is imperative to optimize the photophysical properties of mesoporous templated growth of highly fluorescent perovskite NPs on alternative mesoporous, high aspect ratio nanostructured templates.

During the past decades, mesoporous Si nanowires (NWs) grown by a metal-assisted chemical etching (MACE) method has captured enormous attention due to its fascinating physical and chemical characteristics.[35−39] The MACE process results in the growth of Si NWs with rough side walls due to the lateral etching of NW side wall along with the fast vertical etching, and it results in a mesoporous structure on the Si NWs. The porosity of the NWs can be controlled by simply varying the etching parameters.[35,37,38,40] Interestingly, the high aspect ratio mesoporous Si NWs have been used as a template for the fabrication platform of different nanostructured materials, such as ZnO NCs,[41] Pd NPs,[42] and Au NWs.[43] However, it has not been explored yet for the growth of perovskite NPs. The growth of perovskite NPs on a mesoporous Si NW is not only interesting from the structural point of view but also beneficial from the energetics point of view due to the interesting and tunable optical properties of both the Si NWs and the perovskite NPs. This calls for a detailed investigation of the hybrid system for various emerging applications. The controlled fabrication of perovskite NPs on a Si NW template is highly desirable for various device applications, since Si continues to be the material of choice for robust applications. Wafer-based fabrication methods have a definite edge over the other methods for the practical realization of integrated optoelectronic devices.

Herein, we have investigated the growth of $CH_3NH_3PbI_3$ NPs on mesoporous Si NWs templates grown by the MACE method, for the first time, and explored its photophysical properties. The vertically aligned mesoporous Si NWs array was grown by one-step and two-step MACE of Si wafer using Ag NPs as the noble metal catalyst. Different perovskite precursor solutions were spin-coated on the Si NW array, and postdeposition annealing at 80 °C for 20 min results in the growth of crystalline perovskite NPs at the porous sites of the mesoporous Si NWs. We have controlled the size of the perovskite NPs by controlling (a) the porosity of NWs during the etching process and (b) the concentration of perovskite precursor solution. Highly crystalline perovskite NPs with tunable sizes were formed depending on the perovskite concentration and the pore size of the NWs. We report on the high PL quantum yield (QY) from the perovskite NPs grown on Si NWs as compared to that of the perovskite thin film on a Si wafer. The enhancement of PL intensity is dependent on the nature of NW template. Our study revealed that the decrease in particle size, quantum confinement of carriers in the perovskite NPs, and reabsorption of photon emitted from Si NWs by the perovskite NPs followed by the PL emission are primarily responsible for the large enhancement of PL from the perovskite NPs on mesoporous Si NWs array. UV−vis diffuse reflectance and time-resolved PL (TRPL) studies are presented in support of our claim. This study explores the combined use of microscopic and spectroscopic tools to reveal the mechanism behind the superior photophysical properties of the perovskite NPs grown on a mesoporous Si NW template.

2. EXPERIMENTAL DETAILS

2.1. Materials. All reagents were used as-received without further purification. The purchased reagents are methylamine solution (CH_3NH_3, 33 wt % in absolute ethanol, Sigma-Aldrich), lead(II) iodide (PbI_2, 99%, Sigma-Aldrich), hydroiodic acid (HI, 57 wt % in water, Sigma-Aldrich), *N*,*N*-dimethylformamide (DMF, >99%, Sigma-Aldrich), diethyl ether (>99%, Merck), HF (48%, Merck), H_2O_2 (50%, Merck), $AgNO_3$ (>99.5%, Merck), HNO_3 (69%, Merck), etc.

2.2. Growth of Mesoporous Si NWs. The mesoporous Si NWs were grown by a well-known metal-assisted chemical etching (MACE) method at room temperature using Si wafers as the starting material.[36,37,44] Boron-doped p-type Si (100) wafers with different resistivity (ρ) 0.01, 0.001, and 1 Ω·cm were first cleaned by the typical Radio Corporation of America (RCA) cleaning process.[37] Subsequently, the MACE is performed using either a one-step or a two-step process.[36,37,41] For the two-step process, first a thin layer of Ag NPs was deposited on the Si wafers by dipping it in a solution containing 5.55 M HF and 0.015 M $AgNO_3$ for 5 s. Next, the Ag-coated substrates with resistivity 0.01 Ω·cm were immersed in a solution containing 5 mL of HF (48%), 2 mL of H_2O_2 (50%), and 23 mL of DI water for 20 min (sample NW1), 10 min (sample NW1A), and 5 min (sample NW1B). In the case of the one-step process, the cleaned p-type Si wafers with resistivity 0.01 Ω·cm were immersed into a solution containing 0.015 M $AgNO_3$ and 5.55 M HF for 1 h (sample NW2). We have also performed a two-step MACE for 20 min on Si wafer with resistivity 1 Ω·cm (sample NW1X) and 0.001 Ω·cm (sample NW1Y). A detailed account of the samples is summarized in Table S1 (Supporting Information). In order to remove the residual Ag NPs after etching, all the samples were dipped in 10% HNO_3 solution after growth. Then the samples were removed and rinsed in DI water and dried in Ar gas flow.

2.3. Synthesis of CH_3NH_3I. CH_3NH_3I was synthesized according to the literature report by reaction of 24 mL of methylamine solution (33 wt % in ethanol), 10 mL of hydroiodic acid (HI, 57 wt %), and 100 mL of ethanol in 250 mL round-bottom flask at 0 °C for 2 h with stirring at 400 rpm.[45] Then the precipitate was collected by evaporating the solvent at 60 °C for 3 h. The precipitate was washed three times with diethyl ether and finally collected after recrystallization. Then CH_3NH_3I crystals were dried overnight at 60 °C in a vacuum oven.

2.4. Synthesis of $CH_3NH_3PbI_3$. $CH_3NH_3PbI_3$ was deposited using a conventional single-step deposition method on different Si NW samples (NW1 and NW2) and bare Si wafer. 0.100 g of CH_3NH_3I and 0.250 g of PbI_2 were dissolved in 1 mL of anhydrous *N*,*N*-dimethylformamide (DMF) to produce a clear 22.5 wt % Perovskite precursor (Pe1).[46] We have also prepared 11.2 wt % (Pe2), 5.6 wt % (Pe3), and 2.8 wt % (Pe3) perovskite precursor in DMF (sample codes are summarized in Table S2). The prepared solutions were spin-coated at 2500 rpm for 45 s on different NW templates. After the perovskite deposition, the samples were transferred on a hot plate and annealed at 80 °C for 20 min for the formation of crystalline perovskite layer. The samples were termed with generic code NW*x*Pe*y*, where "*x*" refers to different Si NWs and "*y*" refers to different concentration of perovskite precursor. For example, when Pe1 is coated on NW1, the sample is termed as NW1Pe1 and so on. The perovskite film deposited on bulk Si wafer is referred as Pe on bulk Si. Scheme 1 illustrates the processes involved in the fabrication of the perovskite NPs on the measoporous Si NWs that are grown by a two-step etching process.

2.5. Characterization Techniques. The morphology and elemental compositions of different Si NW samples before and after the perovskite deposition were characterized using a field emission

DOI: 10.1021/acsanm.8b00047
ACS Appl. Nano Mater. XXXX, XXX, XXX−XXX

Scheme 1. Illustration of Growth of Mesoporous Si NWs by a Two-Step Metal-Assisted Chemically Etching (MACE) Process Followed by the Spin-Coating of the Perovskite Layer To Fabricate the Perovskite NPs on the Si NW Template

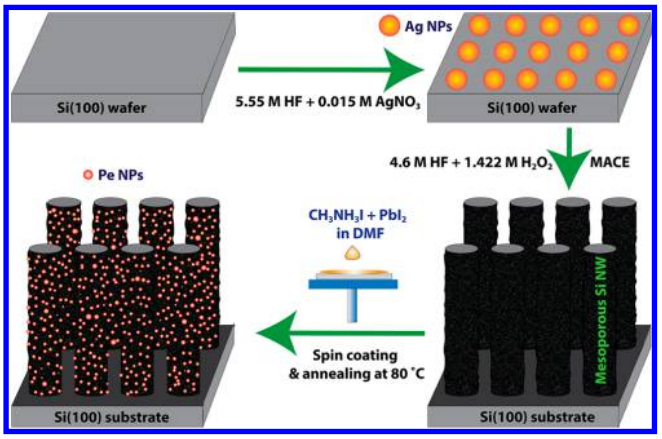

scanning electron microscope (FESEM, Sigma, Zeiss) equipped with an energy dispersive X-ray (EDX) spectrometer. The high-magnification surface morphologies of Si NWs and perovskite NPs for different samples were studied using a transmission electron microscope (TEM) (JEOL-JEM 2010) operated at 200 kV. The samples for TEM analysis were prepared on a carbon-coated Cu grid of 400 mesh (Pacific Grid, USA). STEM-EDS elemental mapping was performed by field emission transmission electron microscope (FETEM) (JEOL-2100F). For structural characterizations, an X-ray diffractometer (XRD) (Rigaku RINT 2500 TRAX-III, Cu Kα radiation) was used for different samples. UV−vis diffuse reflectance spectra (DRS) of the samples were measured using a commercial spectrophotometer equipped with integrating sphere (PerkinElmer, Lamda 950). More details of the DRS measurement are provided in the Supporting Information, section S1.1. The steady-state PL spectrum of different samples was recorded using a 405 nm diode laser (CNI Laser) excitation with the help of a commercial fluorometer (Horiba Jobin Yvon, Fluoromax-4). The photoluminescence quantum yield (PL QY) of the samples was measured with an integrating sphere (FM-SPHERE, Horiba) attached with the fluorometer. Further details of the QY measurement are provided in the Supporting Information, section S1.2. Fluorescence image of perovskite NPs-coated Si NW was taken with a Zeiss LSM 880 confocal microscope with 405 laser excitation. Nitrogen adsorption−desorption isotherms were conducted using a Quanta chrome autsorb-iQ MP analyzer at 77 K. The surface area of the NW was determined using the multipoint Brunauer−Emmett−Teller (BET) method, and the average pore size was determined using the Barett−Joyner−Halenda (BJH) model. Time-resolved PL (TRPL) measurements were performed using a 405 nm pulsed laser excitation, with an instrument time response of <50 ps (LifeSpecII, Edinburgh Instruments). All the measurements including XRD, PL, DRS, and TRPL were carried out in open air atmosphere without humidity control/glovebox. This shows the robustness of the procedure and the obtained results for practical application. Note that in perovskite solar cell and LED the degradation is accelerated due to the presence of different transporting layer and interfaces.[4,47]

3. RESULTS AND DISCUSSION

3.1. Morphology and Structural Analysis. *3.1.1. FESEM and TEM Analysis.* Figure 1 shows the FESEM images of NW1 and NW2 before (first column) and after (second column) the deposition of the perovskite layer. Figures 1a and 1c are the top view and cross-sectional view images of NW1, while Figures 1b and 1d correspond to sample NW1Pe1. Likewise, Figures 1e and 1g are the top view and cross-sectional view FESEM images of NW2, while Figures 1f and 1h correspond to sample NW2Pe1. From the FESEM images, it is evident that the top and side surfaces of the Si NWs are covered by the perovskite NPs (Pe NPs) containing film. FESEM images also reveal that the Si NWs in NW1 are more rough than that in NW2. Note that the porosity of Si NWs and the presence of Pe NP on the Si NW surface are not clearly discernible from the FESEM images due to the resolution limit. From the FESEM image of NW2Pe1, some bigger size Pe NPs are observed, while no such particles were observed on NW1. In order to figure out the elemental composition, we have carried out the EDX analysis. Figure S1a (Supporting Information) shows the EDX mapping and elemental composition of NW1Pe1. Figure S1b shows the elemental composition of NW1Pe1 in the selective portion in Figure S1a. For further confirmation of the elements present and its distribution, the elemental color mappings of the selective portion in Figure S1a are shown in Figure S1c−h. This confirms that the Pe NPs are uniformly coated on the entire surface of Si NW arrays down to the bottom of the NWs.

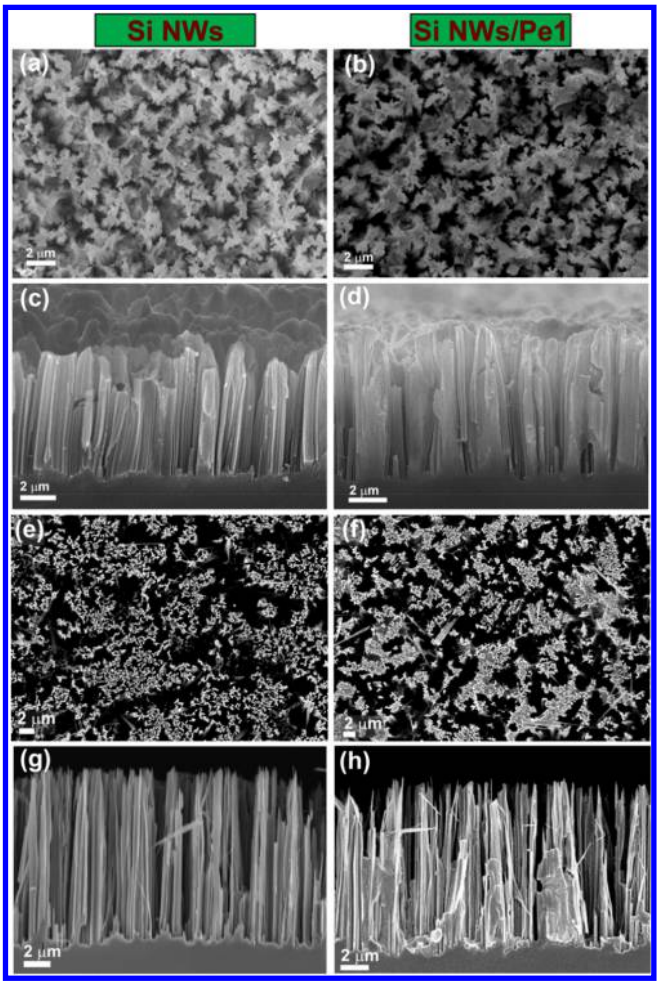

Figure 1. FESEM images of Si NWs before (first column) and after (second column) perovskite deposition: (a, c) top view and cross-sectional view images of Si NWs in NW1; (b, d) top and cross-sectional images of perovskite NPs decorated Si NWs in NW1Pe1, respectively; (e, g) top view images and cross-sectional view of Si NWs in NW2; (f, h) top view and cross-sectional view images of perovskite NPs decorated Si NWs in NW2Pe1.

TEM analysis provides a detailed view of surface morphology of individual Si NW and the formation of Pe NPs nucleated at the pores of the NWs. Figures 2a and 2b show the TEM images

DOI: 10.1021/acsanm.8b00047
ACS Appl. Nano Mater. XXXX, XXX, XXX−XXX

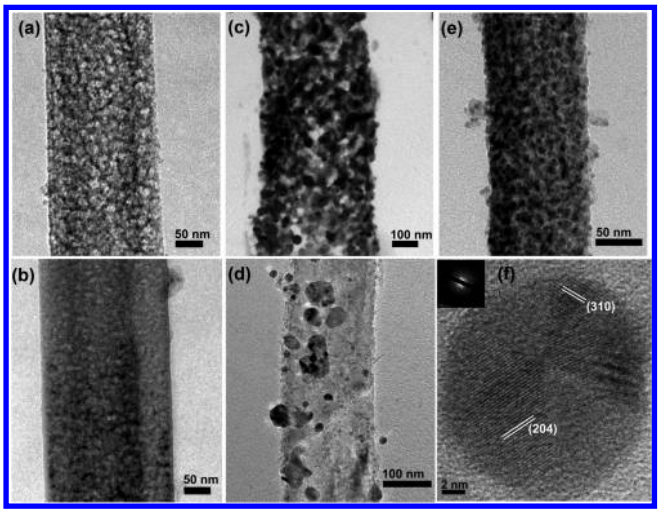

Figure 2. TEM images of bare single Si NW in samples: (a) NW1 and (b) NW2. (c, d) TEM images of perovskite NPs decorated Si NWs in sample NW1Pe1 and NW2Pe1, respectively. (e) TEM image of perovskite NPs decorated on a single Si NW in sample NW1Pe2. (f) HRTEM lattice image of perovskite NPs on NW surface from sample NW1Pe1; the inset shows the SAED pattern, which confirms the crystallinity of $CH_3NH_3PbI_3$ NPs.

of single Si NW in sample NW1 and NW2, respectively. It is clear that the NW surface in each case is mesoporous in nature due to the lateral etching of the NWs during the MACE process. Figures 2c and 2d show the TEM images of a single NW/perovskite heterostructure in sample NW1Pe1 and NW2Pe1, respectively. It is clear that Pe NPs are formed on the surface of Si NWs in each case. Higher magnification images of NW1 and NW1Pe2 surface are shown in Figure S2a. It is clear that the porous sites of the Si NWs acted as the nucleation center for the formation of Pe NPs. The size distributions of Pe NPs on different Si NW are calculated and shown in Figure S3. For NW1Pe1, the size of the Pe NPs varies in the range 5−40 nm with a mean size ∼20 nm, while for NW2Pe1 the size varies in the range 10−70 nm with a mean size ∼35 nm. As confirmed from the TEM images, both the NWs are mesoporous, though the porosity and the roughness of NW1 are much higher than that of NW2. This is due to the stronger side wall etching in the case of two-step MACE in NW1 case. The highly porous and rough surface of NW1 causes formation of the high density Pe NPs on NW1 surface. The size of the NPs on NW2 is bigger than that on NW1, which played a significant role for the enhanced PL intensity and blue-shifted PL from the sample NW1Pe1, as discussed later. Figure 2e shows the TEM image of a single Si NW in sample NW1Pe2, and it is clear that the average size of the Pe NPs is smaller in this case as compared to that of sample NW1Pe1. When the concentration of perovskite precursor is lower, the perovskite starts nucleation at the porous sites of the Si NWs, and as a result, the size of the Pe NPs is of the order of pore size of the Si NWs. Thus, the size of the Pe NPs in sample NW1Pe2 is 1−12 nm (Figure S3c), with an average size of ∼5 nm, which is very much similar to the pore size distribution on Si NWs for the sample NW1. The pore size of the Si NWs is calculated from the BET analysis of sample NW1 and is shown in Figure S4. The details of BET surface area analysis are discussed in section S1.3 of the Supporting Information. However, in the NW/perovskite heterostructure, when the concentration of perovskite precursor is high, the size of the Pe NPs becomes larger than the size of the pores on the NW. Thus, we obtained the larger size Pe NPs for sample NW1Pe1 as compared to sample NW1Pe2. Note that surface of the Si NWs in sample NW2 is much smoother than that of sample NW1, and hence we obtained larger Pe NPs for sample NW2Pe1 as compared to the sample NW1Pe1. Figure 2f shows the HRTEM lattice image of a single Pe NP on the surface of a Si NW for sample NW1Pe1, while the inset represents the corresponding SAED pattern. The lattice fringes and SAED pattern confirm the crystalline nature of the Pe NP grown on the Si NW template. We have observed that the Pe NPs are not fully spherical in shape. Rather, it consists of different facets, and we have indexed different facet planes of crystalline $CH_3NH_3PbI_3$ in the HRTEM image in Figure 2f, which is consistent with the literature.[48] The lattice spacings 0.26 and 0.28 nm correspond to (204) and (310) planes of $CH_3NH_3PbI_3$ crystal. For further confirmation of uniform decoration of Pe NPs on NW and to find the elemental composition of different layers, we have performed STEM-EDS elemental mapping of single NW/perovskite in the sample NW1Pe1. Figure 3a shows the TEM image of an individual Si

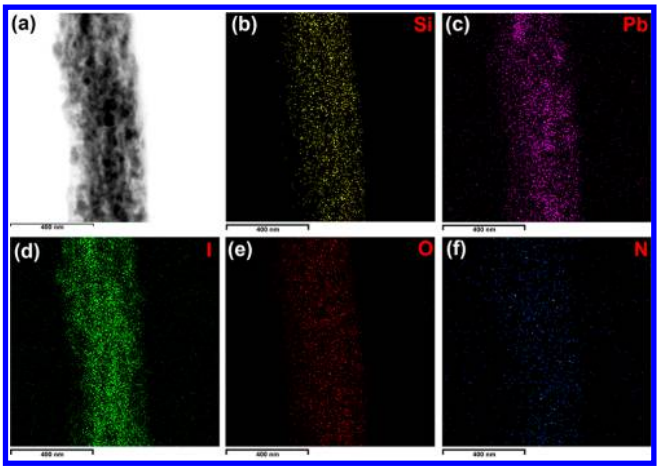

Figure 3. (a) TEM image of individual Si NW/perovskite NPs. (b−f) The corresponding STEM-EDS elemental color mapping of silicon, lead, iodine, oxygen, and nitrogen, respectively.

NW/perovskite NPs, and Figure 3b−f shows the corresponding STEM mapping of different elements that are present in the sample. The mapping very nicely shows the elemental composition of different layers and their distribution. Silicon is observed in side; on top of it oxygen is observed, which is due to the oxide layer on silicon surface. Lead and iodine are observed on the NW surface due to the decoration Pe NPs.

3.1.2. XRD Analysis. The crystal structure and phase of the $CH_3NH_3PbI_3$ were confirmed by X-ray diffraction (XRD) analysis. Figure 4 shows a comparison of the XRD patterns of Pe on silicon wafer along with those of the NW1Pe1 and NW2Pe1. The different XRD peaks of crystalline $CH_3NH_3PbI_3$ were distinguished and well matched with the literature. The strong diffraction peaks at 2θ equal to 14.09°, 19.97°, 23.48°, 24.47°, 28.43°, 31.85°, 34.94°, 40.49°, 43.04°, and 50.18° can be assigned to (110), (112), (211), (202), (220), (310), (312), (224), (314), and (404) crystal planes, respectively.[49] These peaks indicate tetragonal structure of $CH_3NH_3PbI_3$.[49] Figure S5 shows the XRD pattern of the precursor materials PbI_2 and CH_3NH_3I, where the peaks are different from those of the Pe samples. This confirms that the precursor material is

DOI: 10.1021/acsanm.8b00047
ACS Appl. Nano Mater. XXXX, XXX, XXX−XXX

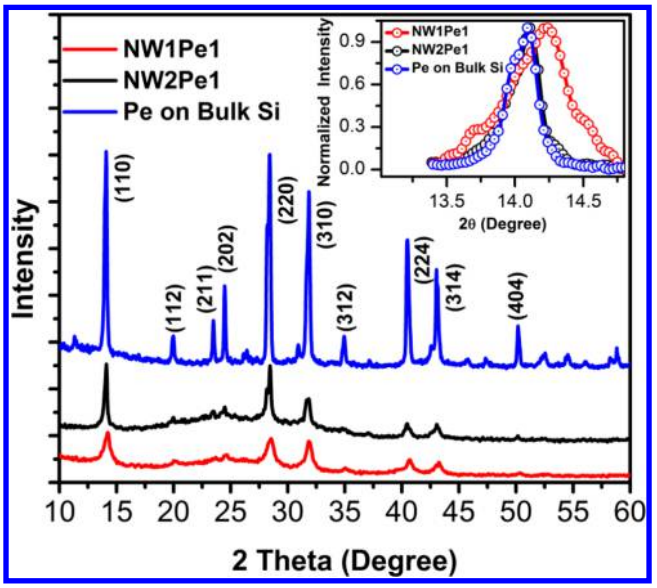

Figure 4. Comparison of XRD patterns of the samples NW1Pe1, NW2Pe1, and perovskite film on Si wafer. The inset shows the normalized XRD pattern of (110) peak for different samples, which indicates the broadening and peak shift in the case of NPs.

completely transformed into the $CH_3NH_3PbI_3$. A broad background peak (2θ = 20°−30°) present in the case of Si NW/perovskite heterostructure is due to the amorphous oxide layer on Si NW.[41] XRD also confirms that the Pe NPs are of the same phase that of the bulk film. In the case of Pe on bulk Si, the intensity of the XRD peak is much higher due to the thicker layer of perovskite. A careful analysis of XRD peak profile indicates that the line width of the XRD peaks is higher in the case of Pe NPs due to the decrease in crystallite size, which indicates the nanocrystalline nature of the Pe NPs.[50] Comparison of normalized intensity of (110) XRD peak is shown in the inset of Figure 4. Interestingly, the broadening of XRD peaks in NW1Pe1 is much higher than that in NW2Pe1, which indicates the formation of smaller size Pe NPs on NW1 than that on NW2. The crystallite sizes of different samples were calculated from (110) peak using Scherrer's formula:[51]

$$D = \frac{k\lambda}{\beta \cos\theta} \tag{1}$$

where k is Scherrer's constant, λ is the wavelength of X-ray of the Cu Kα line (1.54 Å), β is the calculated full width at half-maximum (fwhm), and θ is the Bragg angle. The calculated crystallite sizes for the samples NW1Pe1, NW2Pe2, and Pe on bulk Si are about 16, 34, and 44 nm, respectively. These values are quite consistent with the TEM results discussed earlier. The XRD peaks are slightly shifted toward the higher angle in the sample NW1Pe1 and NW2Pe1, which may due to the compressive strain produced in the Pe NPs on Si NW.[52] We have also calculated the crystallite size and strain in Pe NPs in sample NW1Pe1 using the Williamson−Hall (W−H) plot based on the equation[52]

$$\beta \cos\theta = \frac{k\lambda}{D} + 4e \sin\theta \tag{2}$$

where e represent the strain. Figure S6 shows the W−H plot of sample NW1Pe1. We obtained the crystallite size of 15.9 nm and a compressive strain of 0.088% in sample NW1Pe1, which is consistent with the TEM analysis.

3.2. Diffuse Reflectance Spectroscopy. For a better understanding of the change in band structure of perovskite due to the NP formation, we have carried out the diffuse reflectance spectroscopy (DRS) measurement of various samples, which are opaque in nature. Figure S7a shows the comparison of diffuse reflectance spectra of NW1, NW2, NW1Pe1, NW2Pe1, and Pe on bulk Si along with that of Si wafer. The absorption coefficient/absorbance of a sample is related to the diffuse reflectance (R) by the Kubelka−Munk (K−M) function, $F(R)$, given by

$$F(R) = \frac{(1-R)^2}{2R} = \frac{K}{S} \tag{3}$$

where R is the diffuse reflectance and K and S are the absorption coefficient and scattering coefficient, respectively. Figure 5 shows a plot of the $F(R)$ (K−M function) of the

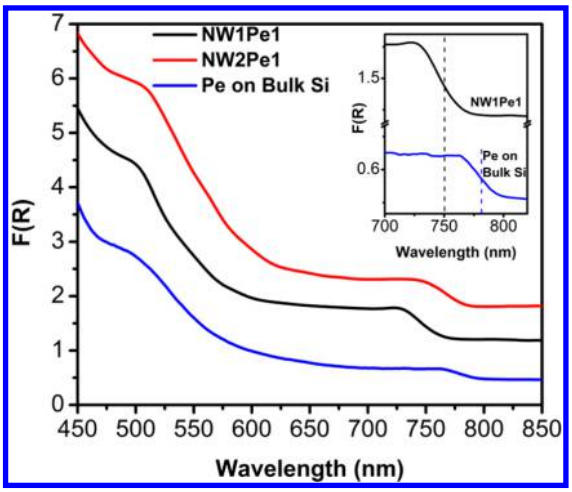

Figure 5. Comparison of the $F(R)$, Kubelka−Munk (K−M) function, for samples NW1Pe1, NW2Pe1, and perovskite film on Si wafer. The inset shows magnified view of the absorption edges indicating blue-shift of the absorption edge for the Pe NPs with respect to that of the Pe film on bulk Si.

samples NW1Pe1, NW2Pe1, and Pe on bulk Si in the range 450−850 nm.[53] It is clear from the figure that all the samples have high absorption coefficient over the entire visible region, and the $F(R)$ increases with decreasing wavelength, as expected for the perovskite layer/NPs.[54] From the K−M plot, it is clear that the absorption coefficient of the samples NW1Pe1 and NW2Pe1 is higher than that of the Pe film on Si wafer. Note that though the absorption coefficient of NW2Pe1 is higher than that of NW1Pe1, the PL intensity (discussed later) of NW1Pe1 is much higher than that of NW2Pe1. The inset of Figure 5 shows a magnified view of the comparison of $F(R)$ for NW1Pe1 and Pe on bulk Si clearing revealing the blue-shift in the absorption edge (indicated by the vertical dashed lines) for the Pe NPs with respect to that of Pe on bulk Si. Interestingly, such a blue-shift indicates the higher bandgap of the Pe NPs, which may be due to quantum confinement effect.[20,25,33,34] Note that the blue-shift is higher for NW1Pe1 as compared to that of NW2Pe1, which reveals a stronger quantum confinement effect in the NPs for NW1Pe1. Dawei et al. showed that the small effective mass of electrons in $CH_3NH_3PbBr_3$ is responsible for the quantum confinement effect, which is observed even at relatively large grain sizes (d > 10 nm), in comparison to the II−VI nanocrystals, such as CdS and CdSe.[25]

DOI: 10.1021/acsanm.8b00047
ACS Appl. Nano Mater. XXXX, XXX, XXX−XXX

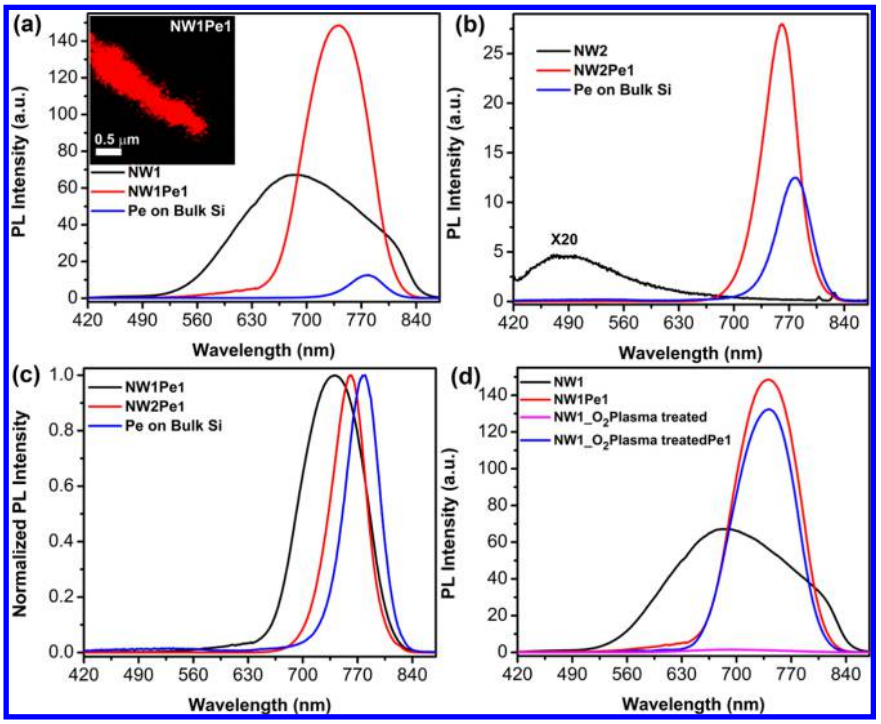

Figure 6. (a) Comparison of PL spectra of the samples NW1, NW1Pe1, and perovskite film on Si wafer; inset shows the fluorescence confocal microscopy image of perovskite NPs-coated single Si NW in the sample NW1Pe1. (b) Comparison of PL spectra of the samples NW2, NW2Pe1, and perovskite film on Si wafer. The PL spectrum of NW2 is magnified by 20 times to enable comparison with the other samples. (c) Normalized PL spectra of NW1Pe1, NW2Pe1, and bulk perovskite film showing blue-shift of peaks for perovskite NPs. (d) Comparison of PL spectra of bare NW1, oxygen plasma treated NW1, and perovskite NPs on NW1 before and after oxygen plasma treatment.

In the present case, the average size of the Pe NPs is ≥10 nm in both NW1Pe1 and NW2Pe1. Figure S7b shows $F(R)$ of the substrates, i.e., bulk Si wafer and bare Si NWs, which reveals that the Si NWs has much higher absorption coefficient than that of the Si wafer. Note that despite the high absorption coefficient of the Si NWs over the entire visible−NIR range, the Pe NPs on Si NWs shows $F(R)$ values lower than that of bare Si NW in the range ∼550−850 nm, implying that the incident light (low intensity) does not penetrate the underlying Si NW layer and the measured spectra are characteristic of Pe NPs with negligible contribution from the underlying Si NWs.

3.3. Steady-State Photoluminescence Study. To study the impact of nanoscale dimension of perovskite on the PL emission, we measured the PL spectra of different samples at room temperature. We have used a 405 nm diode pumped solid-state (DPSS) laser for the excitation of all samples in ambient condition with a constant excitation intensity. The comparison of the PL spectra of the mesoporous Si NW samples before and after Pe NPs decoration is shown in Figures 6a and 6b for NW1 and NW2, respectively. For comparison, the PL spectrum of Pe on bulk Si is presented in each case. Figure 6c depicts the comparison of the normalized PL spectra of sample NW1Pe1, NW2Pe1, and Pe on bulk Si. A single PL peak centered at ∼779 nm was detected in the Pe on bulk Si, which corresponds to the photoemission peak for bulk $CH_3NH_3PbI_3$ perovskite due to the band-to-band transition.[29] The sample NW1 shows a broad (520−850 nm) and high-intensity PL peak. The broad PL emission by MACE grown Si NWs has been well studied and explained based on the following contributions: (a) nonbridging oxygen hole center (NBOHC) defects in the Si/SiO_x interface, (b) the quantum confinement effect in the Si NCs, which are formed due to the lateral etching of the Si NWs, and (c) oxygen vacancy (V_O) defects in the SiO_x structure.[55−57] However, after the decoration of Pe NPs on mesoporous Si NWs, the NW1Pe1 shows enhancement in PL intensity as compared to both bare NW1 and bulk perovskite film. A significant amount of blue-shift (∼38 nm) in the PL peak is observed for sample NW1Pe1 (centered at 741 nm) as compared to the Pe on bulk Si. This type of blue-shift in Pe NPs is attributed to the quantum confinement effect in the Pe NPs, which are formed on the mesoporous surface of the Si NWs.[25,27,28,33] Note that the intensity of the PL peak in sample NW1Pe1 enhances by ∼11.9 times than that of for the Pe on bulk Si. Several factors may be responsible behind the enhancement of PL intensity for the sample NW1Pe1. These are (a) decrease in particle size and the NP formation, (b) quantum size effect in the recombination dynamics of the Pe NPs, (c) reabsorption of photon from mesoporous NWs followed by re-emission by the Pe NPs, and (d) large surface area of the Pe NPs on Si NWs due to the high aspect ratio of the mesoporous Si NWs.

It has been reported that Pe NPs and quantum dots show very high intensity PL emission compared to that of the bulk counterpart due to high radiative recombination in quantum structure.[11,26] In the present case, high density and quantum size Pe NPs are decorated on the surface of the Si NWs. Hence, the quantum confinement effect in Pe NPs is most likely responsible for the huge enhancement in the PL intensity of sample NW1Pe1. Note that sample NW2Pe1 possesses a bigger size and lower density Pe NPs as compared to that of sample NW1Pe1 (as confirmed from the TEM analysis shown in Figure 2c,d). Thus, quantum confinement effect would be less prominent in sample NW2Pe1 as compared to the sample NW1Pe1. As a result, we obtained only 2.2 times enhancement

DOI: 10.1021/acsanm.8b00047
ACS Appl. Nano Mater. XXXX, XXX, XXX−XXX

in PL intensity for NW2Pe1 as compared to that of Pe on bulk Si, as shown in Figure 6b. Because of the larger size Pe NPs, the PL spectrum of NW2Pe1 shows only a 18 nm blue-shift, while it is 38 nm for sample NW1Pe1 from that of the bulk perovskite film (Figure 6c). This is fully consistent with our DRS analysis.

It is also likely that the PL emission intensity of Pe NPs increased partly due to the restricted charge diffusion in smaller size Pe NPs than the bulk Pe crystal case.[26,58] The density of nonradiative centers is directly proportional to the particle size, when the concentration of the luminescent material is unaltered. On the other hand, charge carriers become locally confined within the ultrasmall Pe NPs, and these smaller NP are less affected by the deep trapping sites present in the bigger NPs/bulk crystal.[58] Thus, for a fixed concentration of perovskite, a group of smaller NPs will have higher PL QY as compared to that of the group of larger NPs and bulk perovskite crystals, and this result in higher PL QY from the Pe NPs.

Note that the bare Si NW in NW1 has high intensity PL emission centered at ∼670 nm with a large broadening (in the range of 520−850 nm), as depicted in Figure 6a. The inset of Figure 6a is the fluorescence confocal microscopy image of Pe NPs decorated single NW of the sample NW1Pe1. The perovskite film/NPs has a very high absorbance over the entire visible range as discussed earlier.[4] Thus, Pe NPs can reabsorb the emitted photons by mesoporous Si NWs in NW1Pe1 besides the direct absorption, which may result in high intensity PL from the Pe NPs. Thus, photon recycling phenomenon may be partly responsible for the enhanced PL emission by the Pe NPs in sample NW1Pe1.[53,59,60] Note that the bare Si NWs in NW2 shows very weak PL intensity (Figure 6b) as compared to that in NW1 (I_{NW1}/I_{NW2} = 293). Therefore, the PL intensity enhancement is lesser in NW2Pe1 than that of the NW1Pe1.

To understand quantitatively the amount of PL enhancement in sample the NW1Pe1 due to reabsorption and re-emission, we have further quenched the PL of NW1 by oxygen plasma treatment. In the case of oxygen plasma-treated NW, PL is disappeared due to passivation/removal of NBOHC defects, which is mainly responsible for the PL emission from Si NWs.[57] Figure 6d shows a comparison of the PL spectra of NW1, oxygen plasma-treated NW1, and Pe NPs on NW1 before and after oxygen plasma treatment. After the deposition of perovskite on oxygen plasma-treated NW1, we obtained ∼10.6-fold enhancement in PL intensity, while the enhancement factor was ∼11.9 in the former case (sample NW1Pe1). Therefore, the contribution of photon recycle due to the Si NWs on the PL enhancement of Pe NPs is ∼1.1. Note that there is no change in the spectral shape and peak position of the PL spectra of sample NW1_O_2plasma treatedPe1 as compared to that of for NW1Pe1. Thus, the 10.6-fold enhancement in PL intensity of Pe NPs is only due to the quantum confinement effect of high density Pe NPs on NW surface. We have also measured the PL quantum yield of the Pe NPs in different samples. We obtained PL quantum yields of 9.82%, 2.86%, and 0.69% for NW1Pe1, NW2Pe1, and Pe on bulk Si, respectively, which are considerably high and comparable to the QY reported for $MAPbI_3$ film grown by sophisticated low-pressure vapor-assisted solution process method.[61,62] A summary of the PL features of different samples is presented in Table 1. Digital photographs of the sample NW1Pe1, NW2Pe1, and bulk Pe film on Si wafer under 405 nm laser excitation are shown in Figure S9, which clearly shows that the glow of NW1Pe1 is maximum.

Table 1. Summary of the PL Spectral Features of Different Samples

sample code	PL peak center (nm)	PL intensity enhancement factor with respect to Pe on bulk Si	PL quantum yield (%)
NW1Pe1	741	11.9	9.82
NW2Pe1	761	2.2	2.86
Pe on bulk Si	779	1	0.69

Because of the high aspect ratio of the Si NWs and the multiple reflection in the vertical NW array, a large number of Pe NPs are exposed to the laser excitation. Therefore, the absorption and PL intensity are high in the case of the Si NW/perovskite heterostructure. Note that the effects of quantum confinement of carriers and reabsorption of light are less in the case of sample NW2Pe1, though we observed enhanced PL intensity. This may be due to the larger length of the Si NWs i.e. higher surface area (Figure 1g) of sample NW2. Note that there may be partial quenching of PL intensity from the Pe NPs due to its close contact with the substrate, which may be caused by the possible energy transfer and its influence on the radiative lifetime. Our TRPL data (discussed later) indicate that in the case of Pe NPs contribution of nonradiative energy transfer is less compared to that of Pe film on bulk Si. To study the effect of the substrate on the PL intensity, we have compared the PL spectra of perovskite film on glass and Si substrates for identical thickness. Figure S8 shows the comparison of PL spectra of perovskite films on Si substrate and glass, which shows no significant change in PL intensity for different substrates. To overcome the effect of possible quenching, surface treatment of NWs may be needed and it may lead to higher PL quantum yield.

Next, the full width at half-maximum (fwhm) of the PL spectra was analyzed for different samples. PL spectra of Pe NPs show higher fwhm than that of the Pe film (see Figure 6c). The fwhm for NW1Pe1 and NW2Pe1 are ∼94.6 and ∼51.0 nm, respectively, whereas it is ∼50.1 nm for the Pe on bulk Si. The broad PL peak in NW1Pe1 is due to the wide range of size distribution of the NPs, as confirmed from TEM analysis (Figure S3). Note that there is no considerable difference in the fwhm of PL peak in NW2Pe1 and bulk perovskite film. Hence, the contribution of quantum size effect in sample NW1Pe1 is most significant, which is consistent with our interpretation.

For further confirmation of the size effect and quantum confinement effect in Pe NPs, we have studied the PL spectra of different perovskite heterostructure samples, which are grown with spin-coating of different concentration perovskite precursor on NW1. Figure 7a shows the comparison of PL spectra of samples NW1, NW1Pe1, NW1Pe2, NW1Pe3, and NW1Pe4, while Figure 7b shows the corresponding normalized spectra. The normalized spectrum of Pe on bulk Si is also shown for comparison, which clearly shows large blue-shifts for the smaller Pe NPs obtained with lower concentration of perovskite. For example, with the increasing concentrations of perovskite precursor, the PL contribution of the Si NWs is decreased, and it is minimum for the sample NW1Pe1, where the entire surfaces of the Si NWs is covered by the Pe NPs. As discussed earlier, the Pe NPs start nucleation on the mesoporous sites of the Si NWs, and as a result the surface of the Si NWs is partly exposed to the laser excitation. Hence, the PL contribution of Si NWs is significant to the combined

DOI: 10.1021/acsanm.8b00047
ACS Appl. Nano Mater. XXXX, XXX, XXX−XXX

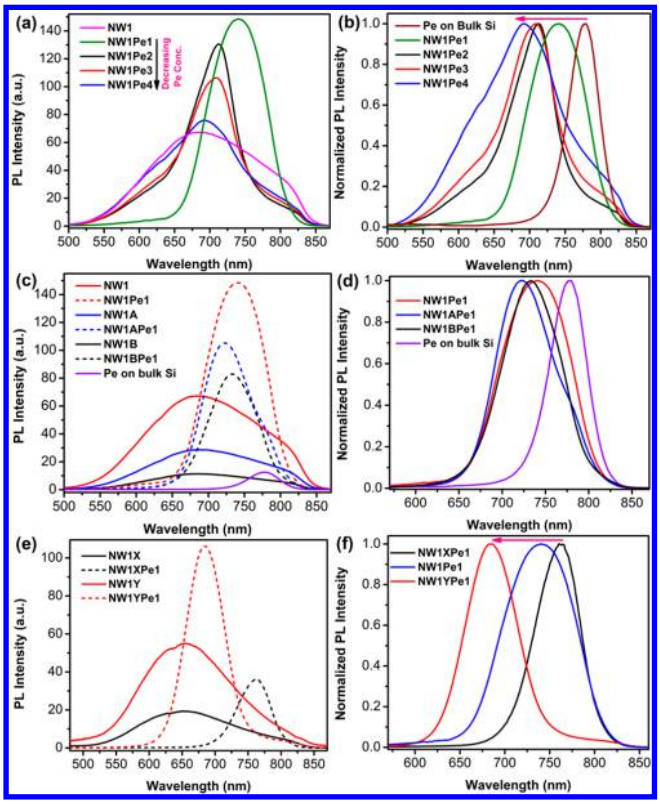

Figure 7. (a) Comparison of PL spectra of NW1/perovskite heterostructure samples for different concentrations of perovskite precursor. (b) Corresponding normalized PL spectra. The normalized PL spectrum of perovskite film on Si wafer is also shown for comparison. (c) Comparison of PL spectra of different bare Si NWs, which are etched for different etching duration with their heterostructure with Pe1. (d) Normalized PL spectra of NW1Pe1, NW1APe1, NW1BPe1, and perovskite film on Si wafer. (e) Comparison of PL spectra of Si NWs, which are grown with different wafer resistivity before and after its heterostructure formation with Pe1. (f) Normalized PL peak of NW1XPe1, NW1Pe1, and NW1YPe1.

spectrum only at lower concentration of perovskite. The density of the Pe NPs and size on Si NWs increases with the increase of perovskite concentration. Therefore, we obtained the systematic enhancement of PL intensity of the Si NWs/perovskite heterostructure samples with the increasing concentration of perovskite. Note that average size of the Pe NPs is smallest when concentration of perovskite is lowest. With the increase in concentration of perovskite, the smaller NPs are merged together and form comparatively larger size NPs. Hence, corresponding to the smallest size NPs in NW1Pe4, we obtained largest blue-shift in the sample, and then it gradually decreases with the increase in concentration of perovskite (Figure 7b). The enhancement in PL intensity and the red-shift of PL peak with the increasing concentration of perovskite precursor are shown in Figure S10a. This further establishes the dominance of quantum confinement (QC) effect in the PL of the Pe NPs.

For a quantitative assessment of the QC effect on the Pe NPs, we used the well-known Brus formula to calculate the blue-shift in band gap from the measured size of the Pe NPs using the relation[63]

$$E_0 = E_g + \frac{h^2}{8\mu R^2} - \frac{1.786e^2}{4\pi\varepsilon_0\varepsilon_r R} \quad (4)$$

which assumes a hydrogen-like model to depict the interaction between electron−hole pairs confined in spherical semiconductor nanocrystals.[63] In eq 4, E_0 is the energy of the lowest excited state of the exciton inside the nanocrystal, E_g is the energy bandgap of bulk $CH_3NH_3PbI_3$ (in our case 1.592 eV), h is Planck's constant, μ is the exciton reduced mass, R is the radius of the nanoparticle, e is the electron charge, and ε_0 and ε_r are the dielectric constants of vacuum and $MAPbI_3$, respectively. The second term in eq 4 corresponds to the first energy level of a quasiparticle of reduced mass μ confined in a spherical well of radius R limited by a wall of infinite potential. Note that in the case of NW1Pe2 the average size of the Pe NPs is ∼5 nm, and using the known values of constants for $CH_3NH_3PbI_3$ ($\mu = 0.08m_0$, $\varepsilon_r = 18$) in eq 4, we estimate a peak shift of 0.158 eV.[29,64] Interestingly, this is very close to the experimentally observed value of 0.150 eV corresponding to the peak at 712 nm (see Figure 7b). This strongly supports the QC model for the observed blue-shift of the PL peak in Pe NPs. In the case of NW1Pe1, the average size of the NPs is ∼20 nm, with some of them in the size <10 nm. Since only the smaller size NPs are expected to contribute toward the blue-shift of the PL peak, taking R = 10 nm in eq 4 yields a calculated blue-shift of ∼0.05 eV, while the experimentally observed blue-shift in 0.08 eV. Such a deviation may hint toward the weak confinement of the NPs due to the larger size NPs in NW1Pe1 as compared to its excitonic Bohr diameter. Note that eq 4 assumes a simple model mostly valid for a strong confinement case. Nevertheless, our calculation provides a convincing evidence for the quantum confinement of carriers in Pe NPs grown on a Si NW template.

In order to understand the effect of surface area on the PL enhancement of NW1/perovskite heterostructure, we have analyzed the PL spectrum of NW1/perovskite heterostructure for two different Si NWs samples etched for different duration (NW1A: etching time 10 min; NW1B: etching time 5 min). Figure 7c shows the comparison of the PL spectra of NW1Pe1, NW1APe1, NW1BPe1, and Pe on bulk Si, while Figure 7d shows the corresponding normalized spectra. The PL spectra of bare Si NWs in sample NW1A, NW1B, and NW1 are also presented in Figure 7c for comparison. Note that NW1 is etched for 20 min for the mesoporous NW formation. As compared to the bulk perovskite film, the PL intensity enhancements in samples NW1Pe1, NW1APe1, and NW1BPe1 are found to be 11.9, 8.4, and 6.7 times, respectively. It is clear that the PL enhancement factor increases with increasing the etching time of Si wafers. Longer etching time leads to the higher length, higher surface area, and higher density of pores on the NW surface. Thus, the PL intensity is higher for sample NW1Pe1 due to the high surface area and higher density of Pe NPs. The change in the PL intensity as a function of NW etching time for different NW/perovskite heterostructure is shown in Figure S10b. The normalized PL spectra of the NW1/perovskite heterostructure shown in Figure 7d reveal a higher blue-shift for the lower etching time for the Si NW formation. For shorter length of Si NWs, the pore density and pore sizes are less as compared to that in longer Si NWs.[39] Thus, during the formation of Pe NPs, the possibility of forming smaller size and isolated Pe NPs is higher in the case of shorter Si NWs with lower density of pores, and it results in the higher blue-shift.

In order to control the size of the Pe NPs on Si NWs, we have controlled the porosity of NW1 by choosing different resistivity (ρ) Si wafers as starting material. Figure 7e shows the

DOI: 10.1021/acsanm.8b00047
ACS Appl. Nano Mater. XXXX, XXX, XXX−XXX

comparison of the PL spectra of bare Si NW sample NW1X (ρ = 1 Ω·cm) and NW1Y (ρ = 0.001 Ω·cm) along with its heterostructure made with Pe1. Figure 7f shows the comparison of the normalized PL spectra of the sample NW1XPe1, NW1Pe1, and NW1YPe1. Note that the resistivity of the starting Si wafer of sample NW1 is 0.01 Ω·cm. With decreasing the resistivity, porosity of the Si NW increases, which causes an increase in the density of smaller size Pe NPs on NW surface. Therefore, we observed higher blue-shift of PL peak for the lower resistivity Si wafer (see Figure 7f).

3.4. Time-Resolved Photoluminescence Study. To gain an insight into the exciton recombination dynamics, time-resolved PL (TRPL) decay of each sample was measured using a pulsed diode laser of 405 nm (average power ~1.0 mW). Figure 8a shows a comparison of the TRPL decay profiles of

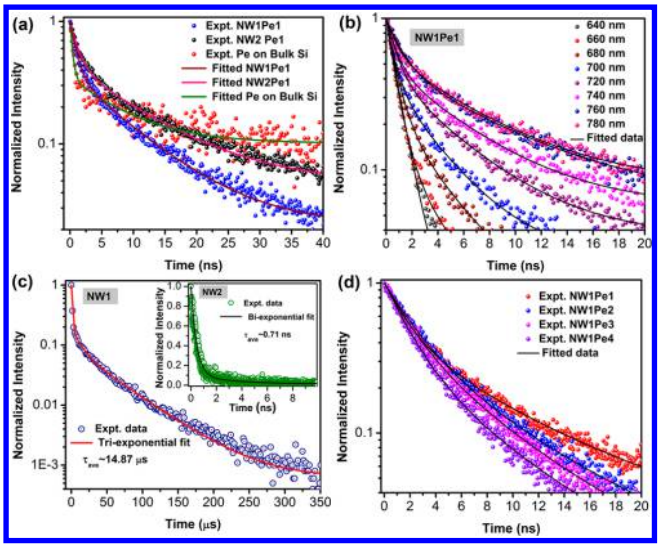

Figure 8. (a) TRPL decay of sample NW1Pe1, NW2Pe2, and perovskite film on Si wafer. (b) PL decay of sample NW1Pe1 at emission wavelengths 640−780 nm, with interval of 20 nm. (c) TRPL decay profile of bare Si NWs in NW1. Inset is the TRPL decay of bare NW2. (d) TRPL decay profiles of the samples NW1Pe1, NW1Pe2, NW1Pe3, and NW1Pe4. In each case, symbols represent the experimental data, and solid lines represent the fitted data.

NW1Pe1, NW2Pe1, and Pe on bulk Si monitored at the PL peak center of each sample. TRPL data in each case were fitted by a biexponential decay function as

$$A(t) = A_1 \exp\left(\frac{-t}{\tau_1}\right) + A_2 \exp\left(\frac{-t}{\tau_2}\right) \quad (5)$$

where $A_1$and A_2 are the amplitudes of the TRPL decay with lifetimes τ_1 and τ_2, respectively. We estimated the average lifetimes (τ_{ave}) using the relation[41]

$$\tau_{ave} = \frac{\sum A_i \tau_i}{\sum A_i} \quad (6)$$

The average lifetimes are found to be 2.44, 3.88, and 5.21 ns for Pe on bulk Si wafer, NW1Pe1, and NW2Pe1, respectively. Thus, as compared to the bulk $CH_3NH_3PbI_3$ film, average recombination lifetimes of Pe NP on Si NWs are higher. This type of prolonged PL lifetime has been observed for $CH_3NH_3PbBr_3$ nanoplatelet, which indicates an extraordinary low nonradiative recombination rate in the perovskite nanoplatelet than the bulk counterpart.[11] It is also observed in mixed halide perovskites.[65] In the present case, the recombination lifetime is higher for Pe NPs, which is due to large radiative recombination than the bulk $CH_3NH_3PbI_3$ film. Thus, the large radiative recombination is the main cause of large PL enhancement in the Si NW/perovskite NPs heterostructure as discussed earlier. Zheng et al. showed that in bulk $CH_3NH_3PbBr_3$ crystal the PL is quenched due to charge trapping.[18] In the present case NW1Pe1 have faster decay than the sample NW2Pe1, which is due to the quantum size effect. Literature reports suggest that in the case of quantum confinement effect smaller NPs have faster TRPL decay than that of larger NPs.[37,66] This is consistent with our interpretation of quantum size effect in Pe NPs.

To study the emission wavelength dependence of PL decay profile, we have measured the decay profiles of NW1Pe1 in the emission wavelength range of 640−780 nm at an interval of 20 nm, and the results are shown in Figure 8b. In each case, the data points are fitted with a biexponential decay, and the fitted curves are shown by the solid lines. Figure 8c shows the TRPL decay profile of bare NW1 fitted by a triexponential decay function, and an average recombination lifetime of ~14.87 μs is obtained. The inset in Figure 8c is the TRPL decay profile of NW2 fitted with a biexponential function with decay lifetime ~0.71 ns. From TRPL analysis (Figure 8b), it is clear that the broad PL peak of NW1Pe1 originates mostly due to different sizes Pe NPs. The decay time constant decreases with increasing the energy of emission. On the basis of the quantum confinement effect, the higher energy PL arises mainly from a group of smaller size NPs, and smaller size NPs have shorter lifetime, as reported in the literature.[37,66] Note that bare NW1 has a very large decay lifetime (~15 μs), which will have negligible contribution to the TRPL decay (in nanoseconds) of NW1Pe1. From the TEM analysis, we observed that the size of the Pe NPs is smaller for lower concentration of perovskite precursor. The TRPL decay profiles of NW1 after the deposition of different concentration of perovskites are shown in Figure 8d. As expected, at lower concentration of the precursor, the decay becomes faster and average recombination lifetime is reduced, which again supports the quantum size effect of the Pe NPs.

This study is significant for the utilization of Pe NPs for the fabrication of PeLEDs, with high PL yield and to overcome the reduced fluorescence efficiency of the clustered Pe NPs. This study demonstrates the fabrication of highly efficient Pe NPs decorated on a versatile platform such as Si NW, which is useful for the LED and light-emitting applications. Note that we prepared the highly photoluminescent Pe NPs on a Si NW template under the ambient condition, without the use of controlled atmosphere usually adopted for such materials and achieved a PL QY of ~10% for the Pe NPs, which is considerably high and comparable to the QY reported for $MAPbI_3$ film grown by sophisticated low pressure vapor-assisted solution process method.[61,62] We believe that the PL QY of our samples can be substantially improved by adopting the fabrication process in a controlled atmosphere and further optimization of the process parameters. The present report may stimulate a thorough investigation on the NW/thin film mesoporous templated growth of Pe NPs and its applications in light-emitting devices, solar cells, etc.

4. CONCLUSIONS

We have investigated the controlled fabrication of $CH_3NH_3PbI_3$ NPs on mesoporous Si NW template for the

DOI: 10.1021/acsanm.8b00047
ACS Appl. Nano Mater. XXXX, XXX, XXX−XXX

first time and reported its high PL quantum yield, which is significant for light-emitting application. Highly crystalline Pe NPs with controlled sizes were synthesized by spin-coating of perovskite precursor on the surface of MACE grown mesoporous Si NWs followed by annealing at 80 °C in ambient condition. Our results demonstrate that the porous sites of the Si NWs act as the nucleation sites for the growth of the Pe NPs. We have tuned the size and PL properties of the Pe NPs by controlling the porosity of the mesoporous Si NWs and perovskite precursor concentrations. The systematic studies by FESEM, TEM, XRD, and EDX confirm that the crystalline Pe NPs are uniformly decorated over the surface of the mesoporous Si NWs. Under ambient condition, the Pe NPs on Si NWs are ∼12 times more PL efficient than the perovskite thin film on Si substrate. It is demonstrated that the ultrasmall size and the quantum confinement effect in the Pe NPs are primarily responsible for the enhanced PL intensity and the blue-shift of PL peak. The reabsorption of photon by Pe NPs from the highly luminescent mesoporous Si NWs followed by the re-emission by the Pe NPs (photon recycling) partly contribute to the PL intensity enhancement of Pe NPs. We achieved a PL QY of 9.82% for the Pe NPs grown on Si NW template under the normal ambient conditions. The systematic studies on Pe NPs by time-resolved PL analysis strongly support our explanation on the origin of PL enhancement in Pe NPs. This study demonstrate the fabrication of Si NWs/perovskite NPs heterostructure, and it unravels the mechanism behind the superior photophysical properties of the Pe NPs decorated on mesoporous Si NWs, which are fabricated by an easy, cost-effective, and novel template based technique. Our results open up the possibility of using perovskite NPs/mesoporous Si NW heterostructure for various kinds of cutting edge applications including LEDs, laser, photovoltaic cells, etc.

■ ASSOCIATED CONTENT

Supporting Information

The Supporting Information is available free of charge on the ACS Publications website at DOI: 10.1021/acsanm.8b00047.

Tables containing sample details of Si NW (Table S1) and perovskite precursors (Table S2); details of diffuse reflectance measurement (section S1.1); details of the PL QY measurement (section S1.2); EDX mapping of NW1Pe1 (Figure S1); TEM image of mesoporous surface of a single Si NW (NW1) (Figure S2a); TEM image of Pe NPs on NW1 in sample NW1Pe2 (Figure S2b); size distribution of Pe NPs in NW1Pe1, NW2Pe1, and NW1Pe2 (Figure S3a−c); N_2 adsorption/desorption isotherms of porous Si NWs obtained from sample NW1 and corresponding BJH pore size distribution (Figure S4a,b); XRD pattern of PbI_2 and CH_3NH_3I power (Figure S5); Williamson−Hall (W−H) plot analysis of sample NW1Pe1 (Figure S6); Vis−NIR diffuse reflectance spectra of NW1, NW2, Si wafer, NW1Pe1, NW2Pe1, and Pe on bulk Si (Figure S7a); Kubelka−Munk plot of the bare Si NWs and Si wafer (Figure S7b); comparison of the PL spectra of perovskite films on bulk Si wafer and glass substrates (Figure S8); digital photographs of the samples NW1Pe1, NW2Pe1, and Pe on bulk Si under 405 nm laser illumination (Figure S9); variation of PL peak intensity and PL peak center for different concentrations of perovskite precursor (Figure S10a); PL intensity of NW1/perovskite heterostructure samples as a function of etching time duration for the growth of Si NWs (Figure S10a) (PDF)

■ AUTHOR INFORMATION

Corresponding Author

*E-mail: giri@iitg.ernet.in (P.K.G.).

ORCID

Joydip Ghosh: 0000-0001-9356-0821

P. K. Giri: 0000-0003-2020-4249

Present Address

R.G.: Department of Physics and Astronomy, Seoul National University, Seoul 151747, Republic of Korea.

Notes

The authors declare no competing financial interest.

■ ACKNOWLEDGMENTS

We acknowledge the financial support from CSIR (Grant No. 03(1270)/13/EMR-II) and MEITY (Grant No. 5(9)/2012-NANO(VOL-II)) for carrying out part of this work. Central Instruments Facility, IIT Guwahati is acknowledged for the FESEM and TRPL facilities.

■ REFERENCES

(1) Correa-Baena, J.-P.; Abate, A.; Saliba, M.; Tress, W.; Jesper Jacobsson, T.; Gratzel, M.; Hagfeldt, A. The Rapid Evolution of Highly Efficient Perovskite Solar Cells. *Energy Environ. Sci.* **2017**, *10*, 710−727.

(2) Zhu, Z.; Bai, Y.; Liu, X.; Chueh, C.-C.; Yang, S.; Jen, A. K. Y. Enhanced Efficiency and Stability of Inverted Perovskite Solar Cells Using Highly Crystalline SnO_2 Nanocrystals as the Robust Electron-Transporting Layer. *Adv. Mater.* **2016**, *28*, 6478−6484.

(3) Park, N.-G.; Grätzel, M.; Miyasaka, T.; Zhu, K.; Emery, K. Towards Stable and Commercially Available Perovskite Solar Cells. *Nat. Energy* **2016**, *1*, 16152.

(4) Yang, L.; Barrows, A. T.; Lidzey, D. G.; Wang, T. Recent Progress and Challenges of Organometal Halide Perovskite Solar Cells. *Rep. Prog. Phys.* **2016**, *79*, 026501.

(5) Lee, Y. H.; Luo, J.; Son, M.-K.; Gao, P.; Cho, K. T.; Seo, J.; Zakeeruddin, S. M.; Grätzel, M.; Nazeeruddin, M. K. Enhanced Charge Collection with Passivation Layers in Perovskite Solar Cells. *Adv. Mater.* **2016**, *28*, 3966−3972.

(6) Mahmood, K.; Swain, B. S.; Amassian, A. 16.1% Efficient Hysteresis-Free Mesostructured Perovskite Solar Cells Based on Synergistically Improved ZnO Nanorod Arrays. *Adv. Energy Mater.* **2015**, *5*, 1500568.

(7) Son, D.-Y.; Im, J.-H.; Kim, H.-S.; Park, N.-G. 11% Efficient Perovskite Solar Cell Based on ZnO Nanorods: An Effective Charge Collection System. *J. Phys. Chem. C* **2014**, *118*, 16567−16573.

(8) Lu, J.; Sheng, X.; Tong, G.; Yu, Z.; Sun, X.; Yu, L.; Xu, X.; Wang, J.; Xu, J.; Shi, Y.; Chen, K. Ultrafast Solar-Blind Ultraviolet Detection by Inorganic Perovskite CsPbX3 Quantum Dots Radial Junction Architecture. *Adv. Mater.* **2017**, *29*, 1700400.

(9) Mali, S. S.; Shim, C. S.; Park, H. K.; Heo, J.; Patil, P. S.; Hong, C. K. Ultrathin Atomic Layer Deposited TiO_2 for Surface Passivation of Hydrothermally Grown 1D TiO_2 Nanorod Arrays for Efficient Solid-State Perovskite Solar Cells. *Chem. Mater.* **2015**, *27*, 1541−1551.

(10) Shi, Z.-F.; Sun, X.-G.; Wu, D.; Xu, T.-T.; Zhuang, S.-W.; Tian, Y.-T.; Li, X.-J.; Du, G.-T. High-Performance Planar Green Light-Emitting Diodes Based on a PEDOT:PSS/$CH_3NH_3PbBr_3$/ZnO Sandwich Structure. *Nanoscale* **2016**, *8*, 10035−10042.

(11) Ling, Y.; Yuan, Z.; Tian, Y.; Wang, X.; Wang, J. C.; Xin, Y.; Hanson, K.; Ma, B.; Gao, H. Bright Light-Emitting Diodes Based on Organometal Halide Perovskite Nanoplatelets. *Adv. Mater.* **2016**, *28*, 305−311.

DOI: 10.1021/acsanm.8b00047
ACS Appl. Nano Mater. XXXX, XXX, XXX−XXX

(12) Jaramillo-Quintero, O. A.; Sanchez, R. S.; Rincon, M.; Mora-Sero, I. Bright Visible-Infrared Light Emitting Diodes Based on Hybrid Halide Perovskite with Spiro-OMeTAD as a Hole-Injecting Layer. *J. Phys. Chem. Lett.* **2015**, *6*, 1883−1890.
(13) Kim, Y.-H.; Cho, H.; Heo, J. H.; Kim, T.-S.; Myoung, N.; Lee, C.-L.; Im, S. H.; Lee, T.-W. Multicolored Organic/Inorganic Hybrid Perovskite Light-Emitting Diodes. *Adv. Mater.* **2015**, *27*, 1248−1254.
(14) Kim, Y.-H.; Cho, H.; Lee, T.-W. Metal Halide Perovskite Light Emitters. *Proc. Natl. Acad. Sci. U. S. A.* **2016**, *113*, 11694−11702.
(15) Cho, H.; Jeong, S.-H.; Park, M.-H.; Kim, Y.-H.; Wolf, C.; Lee, C.-L.; Heo, J. H.; Sadhanala, A.; Myoung, N.; Yoo, S.; Im, S. H.; Friend, R. H.; Lee, T.-W. Overcoming the Electroluminescence Efficiency Limitations of Perovskite Light-Emitting Diodes. *Science* **2015**, *350*, 1222−1225.
(16) Zhu, H.; Fu, Y.; Meng, F.; Wu, X.; Gong, Z.; Ding, Q.; Gustafsson, M. V.; Trinh, M. T.; Jin, S.; Zhu, X. Y. Lead Halide Perovskite Nanowire Lasers with Low Lasing Thresholds and High Quality Factors. *Nat. Mater.* **2015**, *14*, 636−642.
(17) Aygüler, M. F.; Weber, M. D.; Puscher, B. M. D.; Medina, D. D.; Docampo, P.; Costa, R. D. Light-Emitting Electrochemical Cells Based on Hybrid Lead Halide Perovskite Nanoparticles. *J. Phys. Chem. C* **2015**, *119*, 12047−12054.
(18) Zheng, K.; Žídek, K.; Abdellah, M.; Messing, M. E.; Al-Marri, M. J.; Pullerits, T. Trap States and Their Dynamics in Organometal Halide Perovskite Nanoparticles and Bulk Crystals. *J. Phys. Chem. C* **2016**, *120*, 3077−3084.
(19) D'Innocenzo, V.; Srimath Kandada, A. R.; De Bastiani, M.; Gandini, M.; Petrozza, A. Tuning the Light Emission Properties by Band Gap Engineering in Hybrid Lead Halide Perovskite. *J. Am. Chem. Soc.* **2014**, *136*, 17730−17733.
(20) Sichert, J. A.; Tong, Y.; Mutz, N.; Vollmer, M.; Fischer, S.; Milowska, K. Z.; García Cortadella, R.; Nickel, B.; Cardenas-Daw, C.; Stolarczyk, J. K.; Urban, A. S.; Feldmann, J. Quantum Size Effect in Organometal Halide Perovskite Nanoplatelets. *Nano Lett.* **2015**, *15*, 6521−6527.
(21) Schmidt, L. C.; Pertegás, A.; González-Carrero, S.; Malinkiewicz, O.; Agouram, S.; Mínguez Espallargas, G.; Bolink, H. J.; Galian, R. E.; Pérez-Prieto, J. Nontemplate Synthesis of CH3NH3PbBr3 Perovskite Nanoparticles. *J. Am. Chem. Soc.* **2014**, *136*, 850−853.
(22) Chen, J.; Žídek, K.; Chábera, P.; Liu, D.; Cheng, P.; Nuuttila, L.; Al-Marri, M. J.; Lehtivuori, H.; Messing, M. E.; Han, K.; Zheng, K.; Pullerits, T. Size- and Wavelength-Dependent Two-Photon Absorption Cross-Section of CsPbBr3 Perovskite Quantum Dots. *J. Phys. Chem. Lett.* **2017**, *8*, 2316−2321.
(23) Chen, J.; Chábera, P.; Pascher, T.; Messing, M. E.; Schaller, R.; Canton, S.; Zheng, K.; Pullerits, T. Enhanced Size Selection in Two-Photon Excitation for CsPbBr3 Perovskite Nanocrystals. *J. Phys. Chem. Lett.* **2017**, *8*, 5119−5124.
(24) Hintermayr, V. A.; Richter, A. F.; Ehrat, F.; Döblinger, M.; Vanderlinden, W.; Sichert, J. A.; Tong, Y.; Polavarapu, L.; Feldmann, J.; Urban, A. S. Tuning the Optical Properties of Perovskite Nanoplatelets through Composition and Thickness by Ligand-Assisted Exfoliation. *Adv. Mater.* **2016**, *28*, 9478−9485.
(25) Di, D.; Musselman, K. P.; Li, G.; Sadhanala, A.; Ievskaya, Y.; Song, Q.; Tan, Z.-K.; Lai, M. L.; MacManus-Driscoll, J. L.; Greenham, N. C.; Friend, R. H. Size-Dependent Photon Emission from Organometal Halide Perovskite Nanocrystals Embedded in an Organic Matrix. *J. Phys. Chem. Lett.* **2015**, *6*, 446−450.
(26) Longo, G.; Pertegas, A.; Martinez-Sarti, L.; Sessolo, M.; Bolink, H. J. Highly Luminescent Perovskite-Aluminum Oxide Composites. *J. Mater. Chem. C* **2015**, *3*, 11286−11289.
(27) Malgras, V.; Henzie, J.; Takei, T.; Yamauchi, Y. Hybrid Methylammonium Lead Halide Perovskite Nanocrystals Confined in Gyroidal Silica Templates. *Chem. Commun.* **2017**, *53*, 2359−2362.
(28) Malgras, V.; Tominaka, S.; Ryan, J. W.; Henzie, J.; Takei, T.; Ohara, K.; Yamauchi, Y. Observation of Quantum Confinement in Monodisperse Methylammonium Lead Halide Perovskite Nanocrystals Embedded in Mesoporous Silica. *J. Am. Chem. Soc.* **2016**, *138*, 13874−13881.
(29) Anaya, M.; Rubino, A.; Rojas, T. C.; Galisteo-López, J. F.; Calvo, M. E.; Míguez, H. Strong Quantum Confinement and Fast Photoemission Activation in CH3NH3PbI3 Perovskite Nanocrystals Grown within Periodically Mesostructured Films. *Adv. Opt. Mater.* **2017**, *5*, 1601087.
(30) Dirin, D. N.; Protesescu, L.; Trummer, D.; Kochetygov, I. V.; Yakunin, S.; Krumeich, F.; Stadie, N. P.; Kovalenko, M. V. Harnessing Defect-Tolerance at the Nanoscale: Highly Luminescent Lead Halide Perovskite Nanocrystals in Mesoporous Silica Matrixes. *Nano Lett.* **2016**, *16*, 5866−5874.
(31) Arad-Vosk, N.; Rozenfeld, N.; Gonzalez-Rodriguez, R.; Coffer, J. L.; Sa'ar, A. Inhibition of a Structural Phase Transition in One-Dimensional Organometal Halide Perovskite Nanorods Grown Inside Porous Silicon Nanotube Templates. *Phys. Rev. B: Condens. Matter Mater. Phys.* **2017**, *95*, 085433.
(32) Chen, Z.; Gu, Z.-G.; Fu, W.-Q.; Wang, F.; Zhang, J. A Confined Fabrication of Perovskite Quantum Dots in Oriented MOF Thin Film. *ACS Appl. Mater. Interfaces* **2016**, *8*, 28737−28742.
(33) Demchyshyn, S.; Roemer, J. M.; Groiß, H.; Heilbrunner, H.; Ulbricht, C.; Apaydin, D.; Böhm, A.; Rütt, U.; Bertram, F.; Hesser, G.; Scharber, M. C.; Sariciftci, N. S.; Nickel, B.; Bauer, S.; Głowacki, E. D.; Kaltenbrunner, M. Confining Metal-Halide Perovskites in Nanoporous Thin Films. *Sci. Adv.* **2017**, *3*, e1700738.
(34) Zhang, Z.; Wang, M.; Ren, L.; Jin, K. Tunability of Band Gap and Photoluminescence in CH3NH3PbI3 Films by Anodized Aluminum Oxide Templates. *Sci. Rep.* **2017**, *7*, 1918.
(35) Huang, Z.; Geyer, N.; Werner, P.; de Boor, J.; Gösele, U. Metal-Assisted Chemical Etching of Silicon: a Review. *Adv. Mater.* **2011**, *23*, 285−308.
(36) Ghosh, R.; Giri, P. K. Silicon Nanowire Heterostructures for Advanced energy and Environmental Applications: a Review. *Nanotechnology* **2017**, *28*, 012001.
(37) Ghosh, R.; Giri, P. K.; Imakita, K.; Fujii, M. Origin of Visible and Near-Infrared Photoluminescence from Chemically Etched Si Nanowires Decorated with Arbitrarily Shaped Si Nanocrystals. *Nanotechnology* **2014**, *25*, 045703.
(38) Qu, Y.; Zhou, H.; Duan, X. Porous Silicon Nanowires. *Nanoscale* **2011**, *3*, 4060−4068.
(39) Ghosh, R.; Pal, A.; Giri, P. K. Quantitative Analysis of the Phonon Confinement Effect in Arbitrarily Shaped Si Nanocrystals Decorated on Si Nanowires and its Correlation with the Photoluminescence Spectrum. *J. Raman Spectrosc.* **2015**, *46*, 624−631.
(40) Ghosh, R.; Giri, P. K. Efficient Visible Light Photocatalysis and Tunable Photoluminescence from Orientation Controlled Mesoporous Si Nanowires. *RSC Adv.* **2016**, *6*, 35365−35377.
(41) Ghosh, R.; Giri, P. K.; Imakita, K.; Fujii, M. Photoluminescence Signature of Resonant Energy Transfer in ZnO Coated Si Nanocrystals Decorated on Vertical Si Nanowires Array. *J. Alloys Compd.* **2015**, *638*, 419−428.
(42) Sun, X.-H.; Wong, N.-B.; Li, C.-P.; Lee, S.-T.; Kim, P.-S. G.; Sham, T.-K. Reductive Self-assembling of Pd and Rh Nanoparticles on Silicon Nanowire Templates. *Chem. Mater.* **2004**, *16*, 1143−1152.
(43) Wong, T. C.; Li, C. P.; Zhang, R. Q.; Lee, S. T. Gold Nanowires from Silicon Nanowire Templates. *Appl. Phys. Lett.* **2004**, *84*, 407−409.
(44) Peng, K. Q.; Yan, Y. J.; Gao, S. P.; Zhu, J. Synthesis of Large-Area Silicon Nanowire Arrays via Self-Assembling Nanoelectrochemistry. *Adv. Mater.* **2002**, *14*, 1164−1167.
(45) Yang, S.; Zheng, Y. C.; Hou, Y.; Chen, X.; Chen, Y.; Wang, Y.; Zhao, H.; Yang, H. G. Formation Mechanism of Freestanding $CH_3NH_3PbI_3$ Functional Crystals: In Situ Transformation vs Dissolution−Crystallization. *Chem. Mater.* **2014**, *26*, 6705−6710.
(46) Kumar, Y.; Regalado-Pérez, E.; Ayala, A. M.; Mathews, N. R.; Mathew, X. Effect of Heat Treatment on the Electrical Properties of Perovskite Solar Cells. *Sol. Energy Mater. Sol. Cells* **2016**, *157*, 10−17.
(47) Wang, D.; Wright, M.; Elumalai, N. K.; Uddin, A. Stability of Perovskite Solar Cells. *Sol. Energy Mater. Sol. Cells* **2016**, *147*, 255−275.

DOI: 10.1021/acsanm.8b00047
ACS Appl. Nano Mater. XXXX, XXX, XXX−XXX

(48) Yu, J.; Chen, X.; Wang, Y.; Zhou, H.; Xue, M.; Xu, Y.; Li, Z.; Ye, C.; Zhang, J.; van Aken, P. A.; Lund, P. D.; Wang, H. A High-Performance Self-Powered Broadband Photodetector Based on a CH3NH3PbI3 Perovskite/ZnO Nanorod Array Heterostructure. *J. Mater. Chem. C* **2016**, *4*, 7302−7308.
(49) Qiu, J.; Qiu, Y.; Yan, K.; Zhong, M.; Mu, C.; Yan, H.; Yang, S. All-Solid-State Hybrid Solar Cells Based on a New Organometal Halide Perovskite Sensitizer and One-Dimensional TiO_2 Nanowire Arrays. *Nanoscale* **2013**, *5*, 3245−3248.
(50) Ghosh, J.; Ghosh, R.; Giri, P. K. Tuning the Visible Photoluminescence in Al Doped ZnO Thin Film and Its Application in Label-Free Glucose Detection. *Sens. Actuators, B* **2018**, *254*, 681−689.
(51) Chen, J.; Liu, D.; Al-Marri, M. J.; Nuuttila, L.; Lehtivuori, H.; Zheng, K. Photo-Stability of CsPbBr3 Perovskite Quantum Dots for Optoelectronic Application. *Sci. China Mater.* **2016**, *59*, 719−727.
(52) Giri, P. K.; Bhattacharyya, S.; Singh, D. K.; Kesavamoorthy, R.; Panigrahi, B. K.; Nair, K. G. M. Correlation Between Microstructure and Optical Properties of ZnO Nanoparticles Synthesized by Ball Milling. *J. Appl. Phys.* **2007**, *102*, 093515.
(53) Davis, N. J. L. K.; de la Peña, F. J.; Tabachnyk, M.; Richter, J. M.; Lamboll, R. D.; Booker, E. P.; Wisnivesky Rocca Rivarola, F.; Griffiths, J. T.; Ducati, C.; Menke, S. M.; Deschler, F.; Greenham, N. C. Photon Reabsorption in Mixed CsPbCl3:CsPbI3 Perovskite Nanocrystal Films for Light-Emitting Diodes. *J. Phys. Chem. C* **2017**, *121*, 3790−3796.
(54) Tian, Y.; Scheblykin, I. G. Artifacts in Absorption Measurements of Organometal Halide Perovskite Materials: What Are the Real Spectra? *J. Phys. Chem. Lett.* **2015**, *6*, 3466−3470.
(55) Suzuki, T.; Skuja, L.; Kajihara, K.; Hirano, M.; Kamiya, T.; Hosono, H. Electronic Structure of Oxygen Dangling Bond in Glassy SiO_2: The Role of Hyperconjugation. *Phys. Rev. Lett.* **2003**, *90*, 186404.
(56) Walavalkar, S. S.; Hofmann, C. E.; Homyk, A. P.; Henry, M. D.; Atwater, H. A.; Scherer, A. Tunable Visible and Near-IR Emission from Sub-10 nm Etched Single-Crystal Si Nanopillars. *Nano Lett.* **2010**, *10*, 4423−4428.
(57) Ghosh, R.; Imakita, K.; Fujii, M.; Giri, P. K. Effect of Ag/Au Bilayer Assisted Etching on the Strongly Enhanced Photoluminescence and Visible Light Photocatalysis by Si Nanowire Arrays. *Phys. Chem. Chem. Phys.* **2016**, *18*, 7715−7727.
(58) Tian, Y.; Merdasa, A.; Unger, E.; Abdellah, M.; Zheng, K.; McKibbin, S.; Mikkelsen, A.; Pullerits, T.; Yartsev, A.; Sundström, V.; Scheblykin, I. G. Enhanced Organo-Metal Halide Perovskite Photoluminescence from Nanosized Defect-Free Crystallites and Emitting Sites. *J. Phys. Chem. Lett.* **2015**, *6*, 4171−4177.
(59) Woo, J. Y.; Kim, K.; Jeong, S.; Han, C.-S. Enhanced Photoluminance of Layered Quantum Dot−Phosphor Nanocomposites as Converting Materials for Light Emitting Diodes. *J. Phys. Chem. C* **2011**, *115*, 20945−20952.
(60) Saliba, M.; Zhang, W.; Burlakov, V. M.; Stranks, S. D.; Sun, Y.; Ball, J. M.; Johnston, M. B.; Goriely, A.; Wiesner, U.; Snaith, H. J. Plasmonic-Induced Photon Recycling in Metal Halide Perovskite Solar Cells. *Adv. Funct. Mater.* **2015**, *25*, 5038−5046.
(61) Sutter-Fella, C. M.; Li, Y.; Amani, M.; Ager, J. W.; Toma, F. M.; Yablonovitch, E.; Sharp, I. D.; Javey, A. High Photoluminescence Quantum Yield in Band Gap Tunable Bromide Containing Mixed Halide Perovskites. *Nano Lett.* **2016**, *16*, 800−806.
(62) Richter, J. M.; Abdi-Jalebi, M.; Sadhanala, A.; Tabachnyk, M.; Rivett, J. P. H.; Pazos-Outón, L. M.; Gödel, K. C.; Price, M.; Deschler, F.; Friend, R. H. Enhancing Photoluminescence Yields in Lead halide Perovskites by Photon Recycling and Light Out-Coupling. *Nat. Commun.* **2016**, *7*, 13941.
(63) Brus, L. E. Electron−Electron and Electron-Hole Interactions in Small Semiconductor Crystallites: The Size Dependence of the Lowest Excited Electronic State. *J. Chem. Phys.* **1984**, *80*, 4403−4409.
(64) Umari, P.; Mosconi, E.; De Angelis, F. Relativistic GW Calculations on $CH_3NH_3PbI_3$ and $CH_3NH_3SnI_3$ Perovskites for Solar Cell Applications. *Sci. Rep.* **2015**, *4*, 4467.
(65) Zhang, M.; Yu, H.; Lyu, M.; Wang, Q.; Yun, J.-H.; Wang, L. Composition-Dependent Photoluminescence Intensity and Prolonged Recombination Lifetime of Perovskite CH3NH3PbBr3-xClx films. *Chem. Commun.* **2014**, *50*, 11727−11730.
(66) Rinnert, H.; Jambois, O.; Vergnat, M. Photoluminescence Properties of Size-Controlled Silicon Nanocrystals at Low Temperatures. *J. Appl. Phys.* **2009**, *106*, 023501.

DOI: 10.1021/acsanm.8b00047
ACS Appl. Nano Mater. XXXX, XXX, XXX−XXX